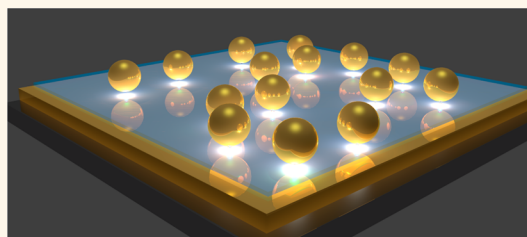


Monitoring Morphological Changes in 2D Monolayer Semiconductors Using Atom-Thick Plasmonic Nanocavities

Daniel O. Sigle,[†] Jan Mertens,[†] Lars O. Herrmann,[†] Richard W. Bowman,[†] Sandrine Ithurria,[‡] Benoit Dubertret,[‡] Yumeng Shi,[§] Hui Ying Yang,[§] Christos Tserkezis,^{||} Javier Aizpurua,^{||} and Jeremy J. Baumberg^{*,†}

[†]NanoPhotonics Centre, Cavendish Laboratory, University of Cambridge, Cambridge, CB3 0HE, United Kingdom, [‡]LPEM, ESPCI-ParisTech, PSL Research University, CNRS, Sorbonne Université UPMC Paris VI, 10 rue Vauquelin, 75005 Paris, France, [§]Pillar of Engineering Product Development, Singapore University of Technology and Design, Singapore 138682, Singapore, and ^{||}Center for Materials Physics, CSIC-UPV/EHU and DIPC, Paseo Manuel de Lardizabal 5, 20018 Donostia-San Sebastian, Spain

ABSTRACT Nanometer-sized gaps between plasmonically coupled adjacent metal nanoparticles enclose extremely localized optical fields, which are strongly enhanced. This enables the dynamic investigation of nanoscopic amounts of material in the gap using optical interrogation. Here we use impinging light to directly tune the optical resonances inside the plasmonic nanocavity formed between single gold nanoparticles and a gold surface, filled with only yoctograms of semiconductor. The gold faces are separated by either monolayers of molybdenum disulfide (MoS₂) or two-unit-cell thick cadmium selenide (CdSe) nanoplatelets. This extreme confinement produces modes with 100-fold compressed wavelength, which are exquisitely sensitive to morphology. Infrared scattering spectroscopy reveals how such nanoparticle-on-mirror modes directly trace atomic-scale changes in real time. Instabilities observed in the facets are crucial for applications such as heat-assisted magnetic recording that demand long-lifetime nanoscale plasmonic structures, but the spectral sensitivity also allows directly tracking photochemical reactions in these 2-dimensional solids.



KEYWORDS: tunable plasmons · 2D-materials · molybdenum disulfide · waveguides · nanoparticles · nano-optics

The nanoparticle on mirror (NPoM) geometry provides unique possibilities to study isolated plasmonic junctions reliably and over a long time.^{1–3} In contrast to individual nanoparticle (NP) dimers,⁴ this geometry allows for simple placement of ultrathin spacer materials into the gap and hence to create stable and well-defined junctions with intriguing materials properties (Figure 1a). Since the discovery of graphene and a range of other 2-dimensional (2D) materials,^{5,6} combining them with plasmonics is of growing interest for a wide range of applications in nano-optoelectronics, quantum information, and biosensing.^{7,8}

The optical scattering spectrum of a NP near a metallic surface consists of several coupled modes. One weaker mode corresponds to transverse dipolar charge oscillations inside the NP alone (*T*).^{7,9–11} However, the dominant modes shift to the red due to longitudinal coupling between the NP and its image in the mirror surface, forming

dipole, quadrupole and higher-order modes.⁹ In the work here, the combination of ultrathin gaps and faceting of the NPs produces nanometer-thick plasmonic cavities in which resonant gap plasmons are confined to form lateral standing waves (of mode index $s = 1, 2, 3, \dots$).^{7,12} The spectral positions of these modes reveal the morphology of the nanostructure and are highly sensitive to small variations of the NP facet sizes. We demonstrate that both semiconductor gap composition and NP morphology can be changed by optical irradiation, thus actively tuning the coupled plasmons as well as tracking few-atom restructurings. The observed metal–insulator–metal (MIM) cavity modes are tightly confined in the nanoscale gaps, but oscillate for many cycles and couple well to incident light, serving as ideal nanoprobe. Studying such atomic instabilities using electron microscopies (such as EELS) is problematic for diameters $>5 \text{ nm}$ ¹³ (see Supporting Information), and

* Address correspondence to jjb12@cam.ac.uk.

Received for review November 10, 2014 and accepted December 15, 2014.

Published online December 15, 2014
10.1021/nn5064198

© 2014 American Chemical Society

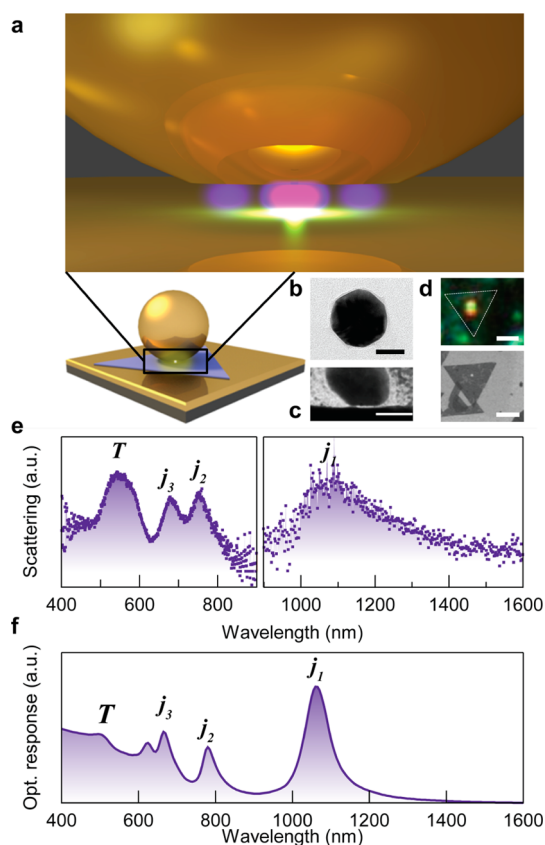


Figure 1. Scattering of NP on mirror with semiconductor nanoplayers. (a) AuNP spaced above gold surface by 2D semiconductor sheet, forming MIM cavity. (b) TEM micrograph of faceted NP (scale bar 50 nm). (c) DF-STEM image of NPoM cross-section. The MIM cavity formed by facet and surface is clearly visible (scale bar 50 nm). (d) DF scattering and SEM of NP on MoS₂ (scale bar 1 μ m). (e) Experimental and (f) Boundary Element Method (BEM) simulation of NPoM optical response. Labeled are resonances arising from hybridized MIM cavity modes ($j_1 j_2 j_3$) and the transverse single NP mode (T).

tends to be invasive as well as only operating in vacuum, precluding *in situ* photochemistry.

RESULTS AND DISCUSSION

The broadband dark-field (DF) scattering spectra of individual 100 nm NPoMs are investigated during irradiation with 448 nm laser light on a 3 μ m diameter spot. Semiconducting spacers of either CdSe nanoplatelets^{1,14,15} with a thickness of 4 atomic layers (which have bandgap at 510 nm), corresponding to a 1.4 nm thick gap, or MoS₂ monolayers (0.65 nm thickness, with bandgap at 690 nm, Figure 1d) are used (see Methods). The scattering of particles placed on top of such sheets can be clearly distinguished from those located directly on the gold surface by their color. The MoS₂ spacer represents a highly robust and inert boundary between AuNP and substrate (as confirmed by Raman scattering) and in contrast to graphene monolayers,⁷ is intrinsically insulating. On the other hand, the CdSe spacer undergoes photochemical

oxidation which enables direct real-time study of the far-field response to variations of the dielectric environment inside the gap.

Surface-enhanced Raman scattering (SERS)^{1,16–20} confirms that all studied AuNPs sit on top of these semiconductor layers (see Supporting Information), which are immersed in the intense enhanced optical fields from the coupled plasmons. Raman scattering from MoS₂-filled gaps is enhanced by >5 orders of magnitude (Supporting Information Figure S2) when resonantly excited at 633 nm while the photoluminescence remains unaffected (Supporting Information Figure S2c).

The dark-field scattering spectra of individual NPoMs exhibit four clear modes (Figure 1e), which match those expected from full electromagnetic simulations (Figure 1f). Using a supercontinuum source and infrared reflecting objective (Methods), we access the spectral range up to 1700 nm. The short-wavelength T mode is accompanied by gap-plasmon modes labeled $j_{1,2,3}$ which theory shows match the lateral standing wave symmetries. Irradiating the NPoM at high angles (using high-NA objectives) accesses the vertical field polarizations of these gap plasmons.⁷ We clearly resolve the more dipole-like mode in the infrared which has a broad line shape because it is radiatively well-coupled. The plasmonic nature of these modes is confirmed by polarization-resolved measurements (Supporting Information Figure S3). Because of the higher noise for $\lambda > 1000$ nm arising from the smaller collection NA and detection efficiency, for the rest of this paper we concentrate on the $j_{2,3}$ modes in the visible/near-IR and employ dark-field refracting objectives.

The NPoM forms a metal–insulator–metal cavity with lateral boundary conditions defined by the facet width (Figure 1c, Figure 2a,b).^{21–23} The basis states in this cavity for in-plane wavevector $k_{||}$ correspond to the MIM waveguide dispersion $E(k_{||})$, which can be calculated for very thin gaps^{24,25} ($d < 10$ nm) giving the effective waveguide refractive index, $n_{\text{eff}} = \hbar c k_{||} / E$ (see Supporting Information eq (S1), Figure S8), dependent on the dielectric constants ϵ_m in the metal and ϵ_d the gap dielectric. The facet width defines lateral discretization of these MIM waveguide modes resulting in solutions of different symmetry within the cavities. In a 1D depiction, the s modes resemble standing waves (Figure 2), as discussed below. For the 2D modes on a circular drum-like facet, this gives approximate solutions for the resonant incident wavelengths $\lambda_i = \pi w n_{\text{eff}} / \alpha_i$ where w is the facet diameter, $\alpha_i = \alpha'_i + \phi_i$ and $\alpha'_i = 3.8, 7.0, 10.2, \dots$ is the i -th antinode of the J_0 Bessel function, while ϕ_i is a phase-shift extracted from the exact simulations.²⁶ The $s = 1$ mode (associated with α_1) is suppressed in large cavities due to charge symmetry considerations (to be reported elsewhere). An even simpler analytic expression

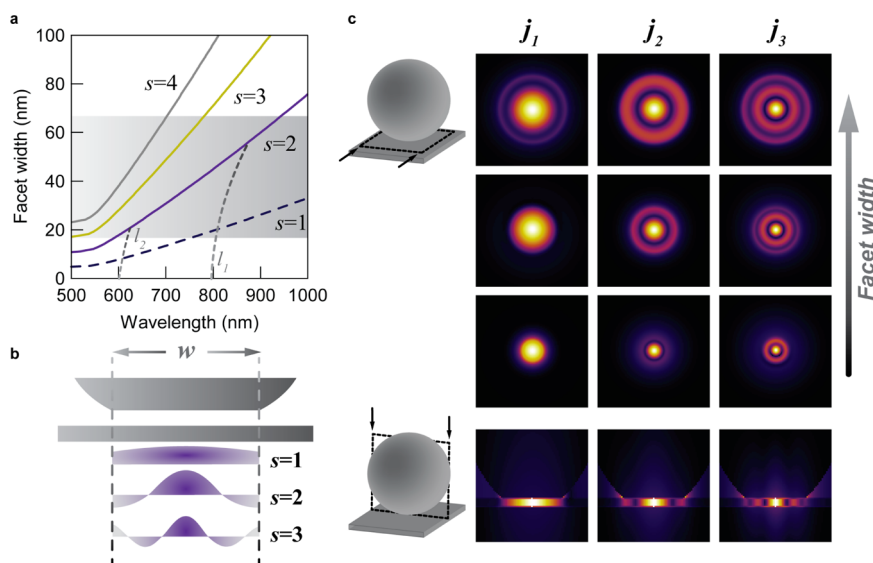


Figure 2. MIM waveguide model. (a) Dispersion of MIM waveguide with $s = 1, 2, 3, 4$ modes for varying facet size. Shaded area shows experimentally accessed facet range. (b) 1D MIM waveguide with boundary conditions defined by the facet size. (c) Lateral normalized field distribution $|E|^2$ for first three modes seen in the nanogap of Figure 1d for increasing facet widths from 10 to 30 nm (top 3 rows) and vertical field distribution of 30 nm facet (bottom).

can be derived if the Drude model for Au is assumed, $\epsilon_m = \epsilon_0 - \lambda^2/\lambda_p^2$, giving

$$\lambda_i \approx \lambda_p \sqrt{\frac{w\epsilon_d}{d\alpha_i} + \epsilon_0} \quad (1)$$

for the resonances (Figure 2a). This estimate gives a good account of the modes observed in Figure 1c,d, and corresponds well to full BEM simulations, showing modes symmetric in z , contrasting to those found in larger gap systems.²¹ It also confirms that the effective refractive index for the MoS₂ NPoM system exceeds $n_{\text{eff}} > 100$ implying that the in-plane wavelength is of order $\lambda_i/n_{\text{eff}} \sim 10$ nm. This explains why these modes can fit within such small facets, which exist on all the Au nanoparticles used here (as in TEM of Figure 1b). For larger facets, the resonant wavelength is larger, producing wider annular field distributions as shown in Figure 2c. We note that these MIM cavity modes (s) efficiently couple to light due to mixing with the matched symmetries of the dipolar ($l = 1$), quadrupolar ($l = 2$) and higher order NP plasmons which act as antennae modes (dashed in Figure 2a). This results in radiative coupling of J_0 transverse modes in the gap (although additional nonradiative J_1 modes are present). This mixing will be dealt with in detail elsewhere, but does not substantively change the broad picture presented. The localized modes evidenced here are thus built from the thinnest waveguide modes yet seen in any system.

Under UV irradiation, red-shifting of these coupled modes ($j_{2,3}$) from single AuNPs on both MoS₂ (Figure 3a) and CdSe (Figure 3b) is observed, while the T modes are not affected. We first irradiate at wavelengths away from the plasmonic resonances although significant field focusing is still present in the nm-gap. The dynamics of the mode shifts depend on the spacer

composition. For MoS₂, the gap modes slowly and monotonically red-shift with irradiation time at a rate $(d/dt)\Delta\lambda_{\text{slow}}^{\text{MoS}_2} = 0.06 \pm 0.04$ nm/s apparently dependent on the exact morphology of the AuNPs.

For CdSe, the slow shifts are also observed under irradiation but are accompanied by an initial much faster red-shifting regime $(d/dt)\Delta\lambda_{\text{fast}}^{\text{CdSe}} = 6 \pm 2$ nm/s which saturates exponentially after ~ 20 s. This fast redshift regime is absent with the MoS₂ spacer.

The sensitivity of this nanomaterial construct to irradiation depends on using the pinhole-free ultrathin semiconductors as structural barriers preventing fusion of the AuNPs and Au substrate. Irradiation excites electrons both in the semiconductor layers and in the local gold surroundings. Since plasmon tunings observed here are irreversible, they do not arise from instantaneous changes in the semiconductor refractive index *via* electronic nonlinearities. Instead, irreversible changes in nanojunction geometry and composition occur through several mechanisms.

The slow red-shift of the plasmonic modes with irradiation can be explained by nanoscale resculpting of the gold atoms around the junction region. Effects of gold mobility have been observed previously for both intense optical²⁷ and thermal²⁸ excitation. Here, both nanoscale optical forces and opto-thermal heating induce a restructuring at the gap, although no global morphology change is apparent in SEMs (despite strenuous efforts because they are so small changes, see Supporting Information). The gap plasmons in the MIM cavity formed by the semiconductor spacer red-shift as the lower NP facet grows (inset Figure 3a), which happens as mobile Au surface atoms are dragged into this ultrathin “optical capacitor” (Figure 3c). We find that no other explanations are capable of accounting for

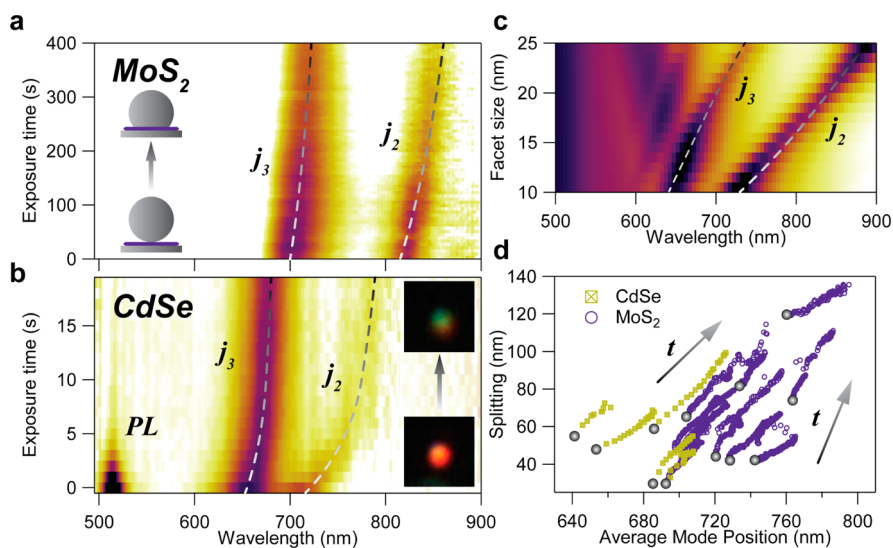


Figure 3. Optical tuning of coupled gap plasmons. (a and b) Scattering spectra of (a) MoS₂ and (b) CdSe NPoM during irradiation with 448 nm laser light. The 514 nm peak in (b) is CdSe photoluminescence. (c) BEM simulation of NPoM optical response with increasing NP facet diameter, showing the *j*_{2,3} modes (dashed). (d) For all different NPoMs, measured spectral splitting $\Delta\lambda = \lambda_2 - \lambda_3$ increases with time compared to average spectral position, for CdSe and MoS₂ spacers. Gray dots indicate beginning of irradiation.

the spectral changes observed, given that the gap material remains intact (see below). For instance alternative tuning effects could arise from local damage of the MoS₂ spacer. This can be ruled out as the SERS and photoluminescence are not affected by optical irradiation, confirming that the integrity of this system is preserved while Au reconstruction takes place. Conducting pinholes would yield blueshifts by discharging the plasmonic gap, thus reducing the strength of the plasmonic coupling. Reorientation of the AuNP facet during irradiation is also unlikely as changes in the scattering would depend strongly on the exact gap morphology whereas the observed phenomena are highly reproducible over hundreds of investigated NPoMs.

With the use of eq 1, the rate of atoms arriving at the facet is

$$\frac{dN}{dt} \approx \frac{\pi\alpha_i w^2 \lambda_i^2}{\lambda_p^2} \cdot \frac{d}{a^2} \cdot \frac{\dot{\lambda}_i}{w_{\text{Ed}} \lambda_i} \quad (2)$$

where the Drude plasma wavelength for Au is $\lambda_p = 154$ nm, and the atomic spacing $a \approx 0.4$ nm (see Supporting Information). This implies that a 1% shift in the *j*₂ mode corresponds to the arrival of 500 atoms onto the facet, or a change in facet radius of less than 1 atom.

These light-induced plasmon shifts are investigated on a range of NPoMs with both MoS₂ and CdSe nanopacers (Figure 3d). The narrower gap formed by 0.7 nm MoS₂ compared to 1.4 nm CdSe, as well as their different out-of-plane permittivities, produces longer wavelength gap modes for MoS₂. This 40% additional red-shift corresponds to significantly greater field enhancement and localization inside the MoS₂ 2D semiconductor sheets. Similar red-shifts under UV irradiation are seen in

all cases, with the spectral separation between *j*₂*j*₃ always increasing. This is expected since confined MIM modes at higher energies sit where the dispersion is flatter (Supporting Information Figure S7) and thus tune less with a change in facet width. For the 30 nm-wide facets seen on most AuNPs here, the tuning rate of λ_2 is predicted to be 40% faster than λ_3 , in line with our measurements. Irradiation with UV deposits energy predominantly in the gold as well as the semiconductor layers, concentrated near the gap by lightning rod effects. Irradiating with a 637 nm pump at identical power levels gives similar (but ~ 10 times slower) red-shifts due to the reduced NPoM cross-section. While independent structural corroboration is inaccessible because these junctions are hidden beneath much bigger nanoparticles, we demonstrate here that optics provides an exquisitely sensitive tool to track material dynamics on the nanoscale. For the 1 nm spectral tracking of the plasmon modes available, we are already sensitive to ~ 10 Au atoms adhering to the facets each 10 ms integration time, and this can be further optimized.

While neither the Raman scattering nor the photoluminescence from the MoS₂-filled gaps are affected throughout the irradiation process, this is not true for the CdSe platelets. Simultaneous with the fast plasmonic red-shift seen at early times when irradiating the CdSe-filled gaps is a decay of the CdSe photoluminescence as well as a decay in the SERS strength of the longitudinal optical (LO) phonon (Figure 3b, Supporting Information Figure S5). Both decays happen on the same time scale and match the faster plasmonic redshift rate. However, the luminescence only decays down to $\sim 15\%$ of its initial value regardless of illumination power suggesting that the CdSe is not ablated in the process

(Supporting Information Figure S5). Further evidence for this comes from rapid shifts in the CdSe LO phonon, commonly attributed to increased strain, and the appearance of a new Raman line near 270 cm^{-1} which is attributed to CdO^{29} (Supporting Information Figure S6). We thus conclude that the fast shift arises from a rapid plasmon-enhanced photochemical reaction in the nanogap of the surface layers oxidizing CdSe to CdO.

Oxidation of the outer CdSe monolayer would lead to a $>100\text{ nm}$ blue-shift jump of the bandgap (since the electrons are more confined inside the remaining inner $\leq 3\text{ ML}$ CdSe), as well as to the observed changes in the Raman scattering. The blue-shifted bandgap is now at higher energy than the excitation laser, thus turning off further excitation.^{6,7} These light-induced modifications of a few hundred semiconductor bonds in the gap lead to changes in the average refractive index (perpendicular to the layers) and to a reduction in the gap size since the relevant *c*-layer lattice constant drops from 6.1 to 4.7 Å in CdO. Modifications of the surrounding ligands are unable to account for our observations as control irradiation measurements with only these ligands (ATP and oleic acid) inside the gap without any platelets do not exhibit such a shift.

CONCLUSION

The potential for plasmon-induced photochemistry thus suggests a powerful way to adapt

metal–semiconductor nanoarchitectures using the resonant tuning of coupled modes together with their optical irradiation. The simple NPoM assembly demonstrated provides a universal base geometry which can be manipulated for a wide variety of 2D semiconductor layers. We demonstrate that optothermal and photochemical reactions involving only few hundred atoms can be tracked in real time using optical scattering at single plasmonic junctions. We show that established MIM models are even applicable for extreme confinement below 1 nm , which is of high relevance for optical circuitry.

This opens up new possibilities for sensing technologies to probe corrosion processes, catalytic reactions, photochemical water splitting, and many other material modifications in extremely confined volumes below a few nm^3 . The ability to track the smallest-scale restructurings in AuNPs potentially allows for the local nanoscale determination of many parameters such as surface energy, adsorption, temperature or roughness at solid–gas or solid–liquid interfaces, as well as directly accessing the dynamics of atom motion. The fact that atoms are mobile under optical irradiation is critically relevant for new developments in heat-assisted magnetic recording (HAMR) for hard-drives,^{30,31} which is emerging as a favored industrial solution to higher areal density storage, as well as for the stability of plasmonic sensing platforms.

METHODS

Sample Preparation. Flat gold layers 70 nm thick were electron-beam-evaporated onto Si wafers. For CdSe nanoplatelet monolayers, the gold surfaces were soaked in 5 mM aqueous 4-aminothiophenol (ATP) for 24 h . The surfaces were dipped in hexane solution with well-dispersed CdSe nanoplatelets for another 24 h . We obtain platelet monolayers with a surface coverage of $\sim 60\%$.

Single crystalline MoS_2 monolayers were grown by chemical vapor deposition (CVD) on a sapphire substrate.³² The MoS_2 monolayer is transferred to a gold substrate using a standard PMMA transfer method.³³

Citrate-stabilized colloidal 100 nm AuNPs in aqueous solution were drop cast onto the sample where surface-binding takes place. After 5 min , excess NP solution was washed away with deionized water.

Experimental Spectroscopy. Optical spectroscopy was performed on a microscope in dark-field (DF) configuration connected to a CCD and using a confocal fiber collection arrangement coupled to a cooled spectrometer. A $100\times$ dark-field objective (Olympus) with collection NA = 0.85 is used, providing excitation through an angular ring around 60° surrounding the collection cone. Intensities used were sufficiently low that no spectral changes were observed without additional laser irradiation. A pump laser (448 nm , 1 mW at sample) is coupled through the same microscope objective to study the irradiation dependence. The resulting power density on the sample is 140 kW/cm^2 given a measured spot size of $\sim 3\text{ }\mu\text{m}$. Control measurements were also carried out with a 637 nm laser with the same power density.

Infrared spectroscopy was performed using a Fianium SC-400 supercontinuum source with power density $\sim 100\text{ kW/cm}^2$ impinging from the side at an angle of 80° and a $40\times$ reflective

infrared objective with NA = 0.5 used for collection of scattered light.

Raman measurements were taken on a Renishaw InVia Raman microscope with resonant excitation of the plasmonic gap mode at 633 nm .

Dark-Field Scanning Transmission Microscopy (DF-STEM) Imaging. First, the NPoM was embedded in a platinum matrix which was evaporated onto the sample surface. A 500 nm thick cross-sectional slab was then isolated from the sample by focused-ion-beam milling, mounted on a TEM grid using a nanomanipulator and polished down to a thickness of $\sim 100\text{ nm}$. DF-STEM imaging was performed in a Hitachi S-5500 SEM at 30 kV acceleration voltage.

Theory Simulations. Exact simulations were carried out using the Boundary Element Method (BEM),^{34,35} with grids sufficiently small to ensure converged solutions in all cases. In the optical response of the NPoM, nonlocal effects are included in our local calculations by conveniently rescaling the separation distances and the dielectric function within the gap, as introduced in Teperik *et al.*³⁶ To that end, the combination of separation distance and dielectric function that best reproduces our experimental results is 0.6 nm for the gap distance and 3.24 for the transverse dielectric function of MoS_2 , matching well the calculated values for monolayer MoS_2 .³⁷ This choice of parameters for the local calculations including nonlocal effects differs from the actual physical values by only a few Angstroms for the separation distance and a few tenths for the refractive index. A similar procedure was adopted for the CdSe layer.

Conflict of Interest: The authors declare no competing financial interest.

Acknowledgment. This work was supported by the UK EPSRC grants EP/G060649/1, EP/L027151/1, Defence Science and Technology Laboratory (DSTL), and ERC grant 320503

LINASS. C.T. and J.A. acknowledge financial support from Project FIS2013-41184-P from MINECO, ETORTEK 2014-15 of the Basque Department of Industry and IT756-13 from the Basque consolidated groups. Experiments were planned and carried out by D.O.S., J.M., L.O.H. and J.J.B. Nanoplatelets were synthesized by S.I. and B.D. MoS₂ samples were fabricated by Y.S. and H.Y.Y. D.O.S., L.O.H., C.T., J.A. and J.J.B. carried out the simulations and developed the theory.

Supporting Information Available: Detailed discussion of the presented waveguide model as well as control experiments supporting the experimental results of this manuscript. This material is available free of charge via the Internet at <http://pubs.acs.org>.

Note Added after ASAP Publication: This paper published ASAP on December 17, 2014. Eq 2 was corrected and additional minor text corrections were made and the revised version was reposted on December 19, 2014.

REFERENCES AND NOTES

- Sigle, D. O.; Hugall, J. T.; Ithurria, S.; Dubertret, B.; Baumberg, J. J. Probing Confined Phonon Modes in Individual CdSe Nanoplatelets Using Surface-Enhanced Raman Scattering. *Phys. Rev. Lett.* **2014**, *113*, 1–5.
- Li, L.; Hutter, T.; Steiner, U.; Mahajan, S. Single Molecule SERS and Detection of Biomolecules with a Single Gold Nanoparticle on a Mirror Junction. *Analyst* **2013**, *138*, 4574–4578.
- Taylor, R. W.; Benz, F.; Sigle, D. O.; Bowman, R. W.; Bao, P.; Roth, J. S.; Heath, G. R.; Evans, S. D.; Baumberg, J. J. Watching Individual Molecules Flex within Lipid Membranes Using SERS. *Sci. Rep.* **2014**, *4*, 1–6.
- Savage, K. J.; Hawkeye, M. M.; Esteban, R.; Borisov, A. G.; Aizpurua, J.; Baumberg, J. J. Revealing the Quantum Regime in Tunnelling Plasmonics. *Nature* **2012**, *491*, 574–577.
- Mas-Ballester, R.; Gómez-Navarro, C.; Gómez-Herrero, J.; Zamora, F. 2D Materials: To Graphene and Beyond. *Nano-scale* **2011**, *3*, 20–30.
- Radisavljevic, B.; Radenovic, a.; Brivio, J.; Giacometti, V.; Kis, a. Single-Layer MoS₂ Transistors. *Nat. Nanotechnol.* **2011**, *6*, 147–150.
- Mertens, J.; Eiden, A. L.; Sigle, D. O.; Huang, F.; Lombardo, A.; Sun, Z.; Sundaram, R. S.; Colli, A.; Tserkezis, C.; Aizpurua, J.; et al. Controlling Subnanometer Gaps in Plasmonic Dimers Using Graphene. *Nano Lett.* **2013**, *13*, 5033–5038.
- Kim, J.; Son, H.; Cho, D. J.; Geng, B.; Regan, W.; Shi, S.; Kim, K.; Zettl, A.; Shen, Y.-R.; Wang, F. Electrical Control of Optical Plasmon Resonance with Graphene. *Nano Lett.* **2012**, *12*, 5598–5602.
- Yamamoto, N.; Ohtani, S.; García de Abajo, F. J. Gap and Mie Plasmons in Individual Silver Nanospheres near a Silver Surface. *Nano Lett.* **2011**, *11*, 91–95.
- Halas, N. J.; Lal, S.; Chang, W.-S.; Link, S.; Nordlander, P. Plasmons in Strongly Coupled Metallic Nanostructures. *Chem. Rev.* **2011**, *111*, 3913–3961.
- Ciraci, C.; Hill, R. T.; Mock, J. J.; Urzhumov, Y.; Fernández-Domínguez, A. I.; Maier, S. A.; Pendry, J. B.; Chilkoti, A.; Smith, D. R. Probing the Ultimate Limits of Plasmonic Enhancement. *Science* **2012**, *337*, 1072–1074.
- Scholl, J. A.; García-ettarri, A.; Koh, A. L.; Dionne, J. A. Observation of Quantum Tunneling between Two Plasmonic Nanoparticles. *Nano Lett.* **2012**, *13*, 564–569.
- Scholl, J. a.; Koh, A. L.; Dionne, J. a. Quantum Plasmon Resonances of Individual Metallic Nanoparticles. *Nature* **2012**, *483*, 421–427.
- Ithurria, S.; Tessier, M. D.; Mahler, B.; Lobo, R. P. S. M.; Dubertret, B.; Efrós, A. L. Colloidal Nanoplatelets with Two-Dimensional Electronic Structure. *Nat. Mater.* **2011**, *10*, 936–941.
- Ithurria, S.; Dubertret, B. Quasi 2D Colloidal CdSe Platelets with Thicknesses Controlled at the Atomic Level. *J. Am. Chem. Soc.* **2008**, *130*, 16504–16505.
- Fleischmann, M.; Hendra, P. J.; McQuillan, A. J. Raman Spectra of Pyridine Adsorbed at a Silver Electrode. *Chem. Phys. Lett.* **1974**, *26*, 163–166.
- Albrecht, G.; Creighton, A. Anomalous Intense Raman Spectra of Pyridine at a Silver Electrode. *J. Am. Chem. Soc.* **1977**, *99*, 5215–5217.
- Moskovits, M. Surface-Enhanced Spectroscopy. *Rev. Mod. Phys.* **1985**, *57*, 783–826.
- Taylor, R. W.; Lee, T.-C.; Scherman, O. A.; Esteban, R.; Aizpurua, J.; Huang, F. M.; Baumberg, J. J.; Mahajan, S. Precise Subnanometer Plasmonic Junctions for SERS with Individual Cross Antennas Tailored to Chemical Moieties. *J. Am. Chem. Soc.* **2013**, *135*, 3688–3695.
- Lassiter, J. B.; McGuire, F.; Mock, J. J.; Ciraci, C.; Hill, R. T.; Wiley, B. J.; Chilkoti, A.; Smith, D. R. Plasmonic Waveguide Modes of Film-Coupled Metallic Nanocubes. *Nano Lett.* **2013**, *13*, 5866–5872.
- Hwang, Y.; Kim, J.-E.; Park, H. Y. Frequency Selective Metal-Insulator-Metal Splitters for Surface Plasmons. *Opt. Commun.* **2011**, *284*, 4778–4781.
- Cai, W.; Wang, L.; Zhang, X.; Xu, J.; de Abajo, F. J. G. Controllable Excitation of Gap Plasmons by Electron Beams in Metallic Nanowire Pairs. *Phys. Rev. B* **2010**, *82*, 125454.
- Kuttge, M.; Cai, W.; García de Abajo, F.; Polman, A. Dispersion of Metal-Insulator-Metal Plasmon Polaritons Probed by Cathodoluminescence Imaging Spectroscopy. *Phys. Rev. B* **2009**, *80*, 033409.
- Bozhevolnyi, S. I.; Søndergaard, T. General Properties of Slow-Plasmon Resonant Nanostructures: Nano-Antennas and Resonators. *Opt. Express* **2007**, *15*, 10869–10877.
- Filter, R.; Qi, J.; Rockstuhl, C.; Lederer, F. Circular Optical Nanoantennas: An Analytical Theory. *Phys. Rev. B* **2012**, *85*, 125429.
- Kuhlicke, A.; Schietinger, S.; Matyssek, C.; Busch, K.; Benson, O. *In Situ* Observation of Plasmon Tuning in a Single Gold Nanoparticle during Controlled Melting. *Nano Lett.* **2013**, *13*, 2041–2046.
- Hugall, J. T.; Baumberg, J. J.; Mahajan, S. Disentangling the Peak and Background Signals in Surface-Enhanced Raman Scattering. *J. Phys. Chem. C* **2012**, *116*, 6184–6190.
- Schaack, G.; Uhle, N. Raman Spectra in Doped Cadmium Oxide. *Solid State Commun.* **1976**, *19*, 315–318.
- Stipe, B. C.; Strand, T. C.; Poon, C. C.; Balamane, H.; Boone, T. D.; Katine, J. A.; Li, J.; Rawat, V.; Nemoto, H.; Hirotsune, A.; et al. Magnetic Recording at 1.5 Pb M-2 Using an Integrated Plasmonic Antenna. *Nat. Photonics* **2010**, *4*, 484–488.
- Challener, W. A.; Peng, C.; Itagi, A. V.; Karns, D.; Peng, W.; Peng, Y.; Yang, X.; Zhu, X.; Gokemeijer, N. J.; Hsia, Y.; et al. Heat-Assisted Magnetic Recording by a near-Field Transducer with Efficient Optical Energy Transfer. *Nat. Photonics* **2009**, *3*, 220–224.
- Lee, Y.-H.; Zhang, X.-Q.; Zhang, W.; Chang, M.-T.; Lin, C.-T.; Chang, K.-D.; Yu, Y.-C.; Wang, J. T.-W.; Chang, C.-S.; Li, L.-J.; et al. Synthesis of Large-Area MoS₂ Atomic Layers with Chemical Vapor Deposition. *Adv. Mater.* **2012**, *24*, 2320–2325.
- Lin, Y.-C.; Zhang, W.; Huang, J.-K.; Liu, K.-K.; Lee, Y.-H.; Liang, C.-T.; Chu, C.-W.; Li, L.-J. Wafer-Scale MoS₂ Thin Layers Prepared by MoO₃ Sulfurization. *Nanoscale* **2012**, *4*, 6637–6641.
- García de Abajo, F.; Aizpurua, J. Numerical Simulation of Electron Energy Loss near Inhomogeneous Dielectrics. *Phys. Rev. B* **1997**, *56*, 15873–15884.
- García de Abajo, F.; Howie, a. Retarded Field Calculation of Electron Energy Loss in Inhomogeneous Dielectrics. *Phys. Rev. B* **2002**, *65*, 115418.
- Teperik, T. V.; Nordlander, P.; Aizpurua, J.; Borisov, a. G. Robust Subnanometric Plasmon Ruler by Rescaling of the Nonlocal Optical Response. *Phys. Rev. Lett.* **2013**, *110*, 263901.
- Davelou, D.; Kopidakis, G.; Kioseoglou, G.; Remedakis, I. N. MoS₂ Nanostructures: Semiconductors with Metallic Edges. *Solid State Commun.* **2014**, *192*, 42–46.